International Journal of Solids and Structures 87 (2016) 254–266

Contents lists available at ScienceDirect

International Journal of Solids and Structures

journal homepage: www.elsevier.com/locate/ijsolstr

Effect of nonlinear multi-axial elasticity and anisotropic plasticity on quasi-static dent properties of automotive steel sheets

Jeong-Yeon Lee[a,b], Myoung-Gyu Lee[a,b,*], Frédéric Barlat[b,c], Kyung-Hwan Chung[d], Dong-Jin Kim[d]

[a] Department of Materials Science and Engineering, Korea University, Seoul 02841, Republic of Korea
[b] Graduate Institute of Ferrous Technology (GIFT), POSTECH, Pohang, Gyeongbuk 37673, Republic of Korea
[c] Center for Mechanical Technology and Automation, Department of Mechanical Engineering, University of Aveiro, 3810-193, Portugal
[d] Product Application Center, POSCO, Incheon 21985, Republic of Korea

ARTICLE INFO

Article history:
Received 16 November 2015
Revised 15 January 2016
Available online 3 March 2016

Keywords:
Dent resistance
Plastic anisotropy
Bauschinger effect
Elastic degradation
Elastic anisotropy

ABSTRACT

This study investigates the influence of the elasto-plastic properties of automotive steel sheets on the denting behavior and suggests a constitutive modeling approach for reliable dent analysis. The stress–strain behaviors of three kinds of steel sheets were measured in uniaxial tension, in-plane biaxial tension and forward-reverse simple shear tests. Advanced constitutive models were employed to capture the plastic anisotropy, reverse loading characteristics such as the Bauschinger effect, and elastic modulus degradation. In particular, the biaxial elastic modulus and its degradation behavior were measured and implemented in the constitutive model. The suggested model significantly improved the prediction of dents compared to the conventional model in terms of the load-displacement curve. Sensitivity studies on the constitutive model demonstrated that mainly plastic anisotropy and elastic behavior of a material influence the panel stiffness, whereas the reverse loading behavior strongly affects the permanent dent depth.

1. Introduction

Panel stiffness and dent resistance are two important quality criteria for automotive outer panels. These properties indicate the ability of a panel to withstand denting under the application of an external load. Automotive denting occurs frequently during the lifetime of a vehicle, including incidents such as hail damage and door-to-door impact, but it is also a concern in the handling of parts during manufacturing. The accurate assessment of panel stiffness and dent resistance is necessary to ensure the robustness of a formed panel throughout the lifetime of the component.

These properties depend strongly on the mechanical properties of the sheet, the deformation paths undergone during forming, panel geometry, and the supporting and external loading conditions. Therefore, with newly designed panel shapes or substitute materials, the stiffness and dent properties must be examined again. This is particularly important considering the current replacement of conventional mild steels by high strength steels (HSS) or advanced high strength steels (AHSS) with reduced thickness for lightweight vehicles.

The direct measurement of dent properties is expensive in cost and time, because a complete toolset is required to form each trial shape. For this reason, a number of empirical relationships have been suggested to correlate dent resistance to the influencing factors. Usually, the static dent energy or dent load has been expressed as a function of elastic properties, yield strength, panel thickness and geometric factors (Dicello and George, 1974; van Veldhuizen et al., 1995). However, these simple expressions are only valid for limited cases, because they ignore the coupling effect among the influencing factors. One example of the coupling effects is that the change of panel curvature affects the amount of plastic deformation applied to the sheet, altering both the yield strength and panel thickness. Moreover, the effects of complex geometry and supporting condition of a real automotive part cannot be sufficiently represented by the few parameters appearing in the proposed empirical relationships. Consequently, these empirical equations are unsuitable to quantitatively assess the dent properties of a panel.

* Corresponding author at: Department of Materials Science and Engineering, Korea University, Seoul 02841, Republic of Korea. Tel.: +82 2 3290 3269.
E-mail addresses: myounglee@korea.ac.kr (M.-G. Lee), f.barlat@postech.ac.kr (F. Barlat).

http://dx.doi.org/10.1016/j.ijsolstr.2016.01.020
0020-7683/

Finite element (FE) analysis allows a realistic modeling of forming and denting procedures, enabling a more reliable assessment of dent properties. However, a proper constitutive description of the sheet is necessary for accurate simulations. First, the plastic anisotropy of the sheet should be described, because automotive outer panels are generally formed under biaxial stress conditions. For this reason, the quadratic anisotropic Hill yield criterion (Hill, 1948) has been used for dent simulations (Holmberg and Nejabat, 2004; Shen et al., 2010). Second, the reverse hardening behavior, such as the Bauschinger effect, needs to be considered, because the sheet may experience reverse loading when a dent occurs on a curved panel. FE simulations using the Chaboche nonlinear kinematic hardening model (Chaboche, 1986) revealed that the description of the Bauschinger effect significantly influenced dent predictions (Shen et al., 2010).

The elastic properties of the sheet are also an important factor because elastic deformation dominates the denting process. When a dent load of 200 N is applied to a dome-stretched steel panel, the permanent dent depth is only 0.2 mm, whereas the maximum deflection of the panel is 7.7 mm (SAE, 2004). This suggests that nearly 97% of the total deflection is elastically recovered when the load is removed. Previous dent studies have assumed a constant value of Young's modulus measured in uniaxial tension tests, usually in the rolling direction (RD) of the sheet. However, experiments on steel sheets have revealed elastic anisotropy and the reduction of the apparent elastic modulus or so-called chord modulus with accumulated plastic deformation (Eggertsen et al., 2011; Sun and Wagoner, 2011). The variation in the initial elastic modulus from the rolling to transverse direction of the sheet is usually 5–10% for steels (Eggertsen et al., 2011). The reduction of chord modulus, as a result of plastic deformation, is about 15–25% for steels, and this phenomenon is mainly attributed to the repulsive interactions between piled-up dislocations (Cleveland and Ghosh, 2002). Therefore, it is necessary to investigate the influence of elastic properties on dent prediction and to determine whether the use of the conventional Hooke's law is appropriate in these analyses.

This study aims to understand the deformation mechanisms undergone by the sheet throughout the forming and denting processes and to suggest a constitutive modeling approach for reliable dent analysis. Three kinds of steel sheets were selected for this study: deep drawing quality (DDQ), bake-hardenable (BH340) and dual-phase (DP490) steels, which are used for automotive outer panels. The stress–strain behaviors of the materials were measured under different loading conditions using uniaxial tension, in-plane biaxial tension and forward-reverse simple shear tests. Advanced constitutive models were employed to describe the measured stress–strain responses in terms of plastic anisotropy, reverse loading behavior and elastic modulus degradation. The adopted models are the non-quadratic anisotropic yield function Yld2000-2d (Barlat et al., 2003), the anisotropic hardening model based on distortional hardening, so-called HAH (Barlat et al., 2011), and strain-dependent elasticity models (Yoshida et al., 2002). The suggested constitutive model was verified using the standard dent test applied in the automotive industry (SAE, 2004), in which the geometry, loading and boundary conditions are precisely defined to minimize experimental scattering or prediction errors caused by factors other than the material properties. This study concerns only quasi-static denting, in which the indenter velocity is slow enough to ignore the strain rate effect.

Section 2 presents a preliminary numerical study on the standard dent test and investigates the deformation mechanism of the sheet. Section 3 describes the experimental procedures for the stress–strain measurement and Section 4 reviews the abovementioned constitutive models. Section 5 presents the verification of the suggested model in the standard dent test and the sensitivity analysis on the influence of material properties. Section 6 demonstrates the usefulness of the standard dent test as a verification example for the abovementioned constitutive models. Finally, Section 7 gives the conclusions and suggestions for future work.

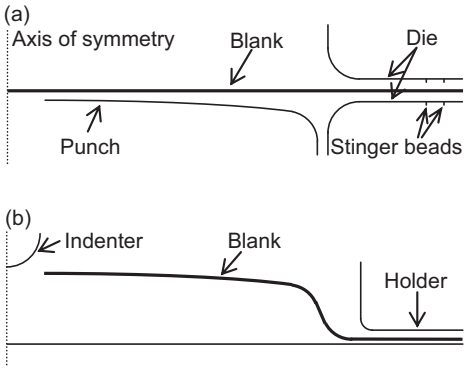

Fig. 1. Schematic for the standard dent test with a dome-stretched panel for (a) pre-stretching and (b) denting. Dimensions are provided in Appendix A.

Table 1
Summary of FE mesh optimization for the standard dent test. Both shell and solid elements are first-order and use reduced integration.

	Shell	Solid
Mesh size in the central region ($r = 50$ mm)	0.1 mm	0.1 mm
Mesh size in the other region	1–3 mm	0.25 mm
Number integration points through thickness	9	–
Number of mesh through thickness	–	7
Relative computation time	1	5.3

2. Preliminary study on the standard dent test

A preliminary FE simulation of the standard dent test (SAE, 2004) was conducted to observe the deformation history of the material through the forming and denting processes. The simulation assumed simple material models, namely, the von Mises yield criterion, isotropic hardening and a constant elastic modulus, using the uniaxial tension data of BH340.

The test procedure consists of two steps, as schematically illustrated in Fig. 1. A 305 mm × 305 mm flat square sheet is formed into a dome-stretched panel with a punch stroke of 12 mm, which results in about 2% biaxial strain prior to denting. Next, the panel is fixed by a holder, subjected to denting using a spherical indenter of 25.4 mm diameter, and unloaded. The tool geometry is described in detail in Appendix A. The standard procedure recommends an incremental increase of the dent load with successive loading-unloading cycles but, for simplicity, only a single loading of 200 N is considered in this study.

A FE model for the dent test was constructed in Abaqus/Standard (implicit) version 6.12. One-quarter of the whole geometry was considered. The tools were modeled using analytical rigid surfaces. Different mesh sizes were assigned in two regions of the sheet: the central region with a radius of 50.8 mm (twice the radius of the indenter) required a fine mesh because the dent was localized in this region, but a relatively coarse mesh was used for the rest. The mesh option was optimized for both shell and solid elements through a series of convergence tests, as summarized in Table 1. The solid and shell elements yielded similar simulation results in terms of the dent profile as well as the load-displacement response of the indenter. This is because the plane stress state dominates during both the forming and denting processes, allowing the stress in the thickness direction to be safely ignored. (It is worth noting that this distinguishes the

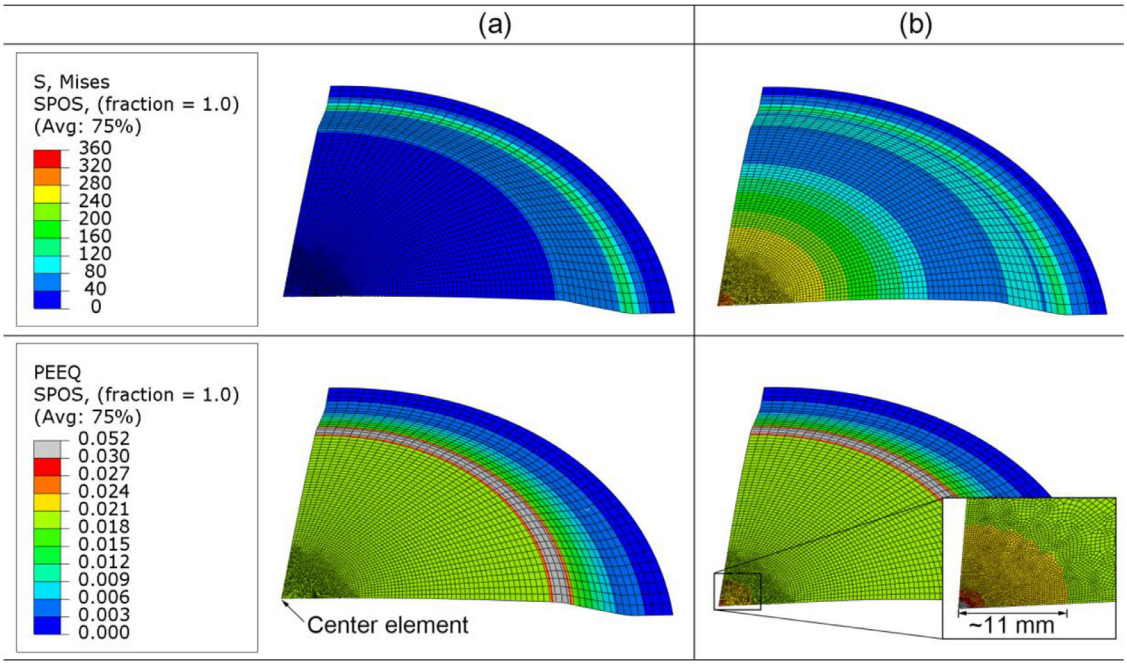

Fig. 2. Predicted von Mises equivalent stress (in MPa) and strain contours on the top surface (a) before denting and (b) under the dent load of 200 N.

deformation characteristics between the denting and indentation of a sheet, as the latter involves significant through-thickness stress.) Because of this similarity, shell elements (S4R in Abaqus) were used for further simulations for computational efficiency. Note that a very fine mesh as small as 0.1 mm is necessary in the dent region, as shown in Table 1.

The friction coefficient was assumed to be 0.2 for all of the contact between the sheet and the tools. This value is considered appropriate for non-lubricated conditions, as in the actual tests. A sensitivity study on the friction coefficient in the range between 0 and 0.2 revealed that the simulation results are rarely affected by the friction coefficient. The hard contact condition was imposed to prohibit the overclosure of the sheet and tool surfaces because this can directly influence the displacement and load predictions of the indenter.

Fig. 2(a) shows the predicted stress and strain distributions of the pre-stretched and unloaded sample before denting. The von Mises equivalent quantities are shown in the figure, where the tools are removed from the display for better visibility. The residual stress is negligible and the pre-strain is uniform in the dome plateau at this stage. Fig. 2(b) shows the same plots under the dent load of 200 N. The equivalent strain distribution at this stage shows that additional plastic deformation due to denting is limited to a small central region, in which the total accumulated plastic strain is less than 3% on average. The rest of the panel deforms only elastically during denting. The plastic strain is higher around the dome corners but less than 10%. The stress and strain quantities shown in Fig. 2 were calculated on the top surface, which is in contact with the indenter, and those on the bottom surface are slightly different.

Furthermore, the entire stress history of an element located at the center of the specimen was observed. Fig. 3(a) and (b) shows the history on the top surface for the pre-stretching and denting processes, respectively. The numbers in the figures indicate the sequence of stress history; for instance, the material on the top surface first experiences biaxial tension during forming (points 1–3), is unloaded (points 3 and 4), subsequently undergoes biaxial compression during denting (points 4–6), and is finally unloaded (points 6 and 7). The elastic loading and unloading responses are also in the balanced biaxial state. Points 4 and 6 in Fig. 3(b) correspond to the states shown in Fig. 2(a) and (b), respectively. The material on the bottom surface, in contact with the punch, does not experience reverse loading, because plastic deformation occurs in biaxial tension during both forming and denting, as shown in Fig. 3(c) and (d). The neighboring elements, which are not at the center but within the dent region, do not follow the exact balanced biaxial condition but between the balanced biaxial and plane strain modes.

These observations suggest that the constitutive model for dent analysis needs to consider the following aspects:

- Elastic behavior, especially in the biaxial state
- Plastic anisotropy
- Monotonic and reverse hardening behaviors

The hardening behaviors of the materials should be carefully measured and described at small plastic strains (less than 10%), as mentioned above.

3. Stress–strain measurement

3.1. Materials

This study used several candidate steel sheets for automotive outer panels. DDQ is an ultra-low carbon interstitial-free steel, classified as mild steel, with high formability. BH340 is an HSS with superior dent resistance compared to mild steels because of the bake-hardening effect. DP490, an AHSS, exhibits the highest strength of the tested materials, while maintaining sufficient formability. The DP490 sheets used in this work were produced at a custom order for manufacturing automotive door panels, and exhibit slightly lower yield strength and higher elongation than the other DP490 products of the same manufacturer. All of the sheets were provided with the same thickness of 0.7 mm.

3.2. Uniaxial tension and unloading tests

Uniaxial tension tests were performed using a Zwick/Roell tensile testing machine. The specimens were fabricated according to the ASTM E8 standard along 0°, 45° and 90° from the RD

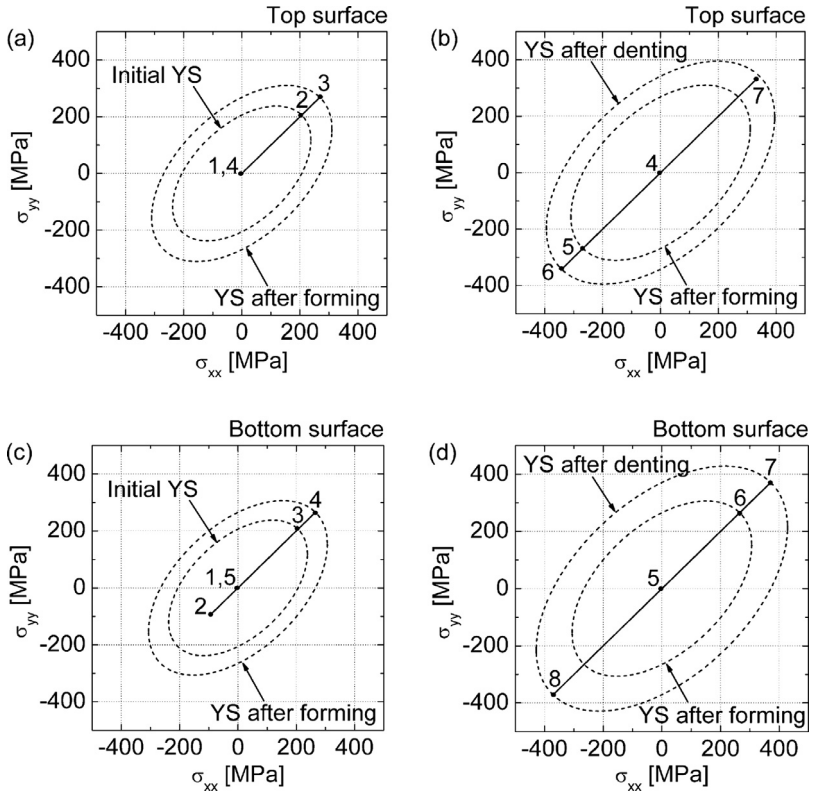

Fig. 3. Stress history of the center element on the top surface during (a) pre-stretching and unloading and (b) denting and final unloading. Similarly, (c) and (d) show the stress history on the bottom surface. Numbers indicate the sequence of the stress history. YS: yield surface.

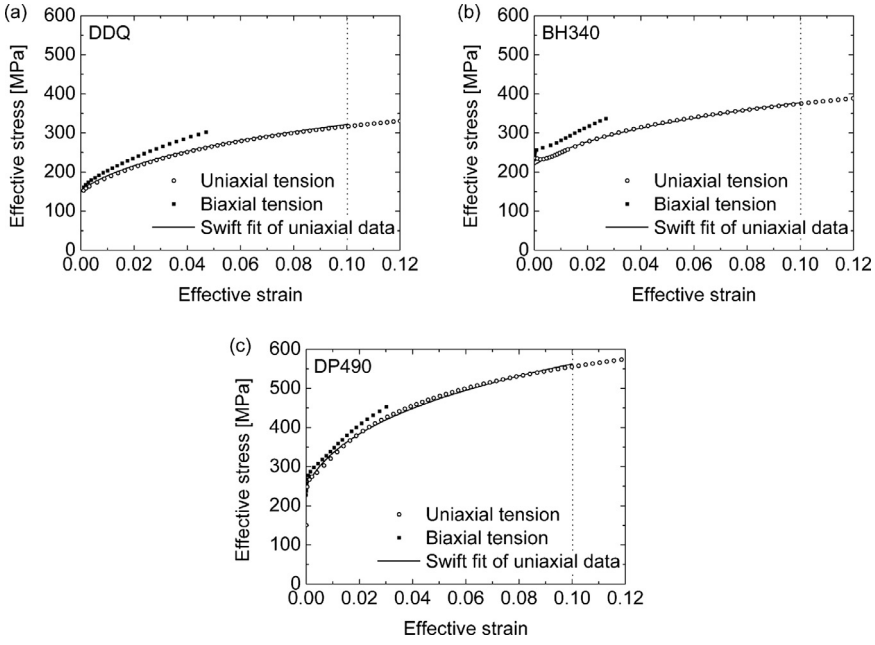

Fig. 4. Effective stress–strain curves measured in uniaxial and balanced biaxial tension for (a) DDQ, (b) BH340 and (c) DP490.

Table 2
Mechanical properties of the steel sheets.

	E_0[a] (GPa)	ν[b]	σ_0[c] (MPa)	σ_{45}[c] (MPa)	σ_{90}[c] (MPa)	σ_b (MPa)	r_0	r_{45}	r_{90}	r_b
DDQ	207	0.3	152	158	155	161	1.50	1.51	1.80	1.83
BH340	216	0.3	236	239	220	262	1.60	0.96	1.62	1.62
DP490	207	0.3	264	262	264	278	0.77	0.92	0.99	1.29

[a] Measured in uniaxial tension along the RD.
[b] Assumed.
[c] 0.1% offset.

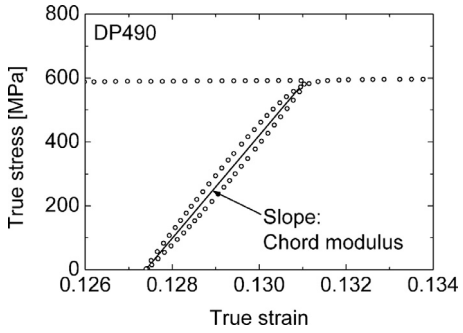

Fig. 5. True stress–strain curve of DP490 measured in uniaxial loading–unloading–reloading. One cycle at a plastic strain of 0.127 is shown in this figure.

(ASTM 2010). The measured stress–strain curves of all three materials are shown in Fig. 4. The basic mechanical properties obtained from these curves are given in Table 2. The uniaxial yield stresses were determined using the 0.1% offset method and r-values were taken at 15% plastic strain The use of the 0.1% offset instead of the typical 0.2% allowed the definition of the initial yield stress closer to the border of the linear elastic region. The r-values tend to saturate quickly within 2–4% plastic strain for all of the materials.

Uniaxial loading–unloading–reloading tests were conducted using the same test setup. The unloading–reloading cycles, such as that shown in Fig. 5, were imposed at different amounts of plastic strain. For each unloading cycle, the chord modulus was determined as the slope of the straight line connecting the starting and ending points of the unloading stress–strain curves (see Fig. 5). The initial and chord moduli are plotted in Fig. 6 as a function of effective strain for the three loading directions of RD, diagonal direction (DD) and transverse direction (TD). As shown in the figure, the chord modulus is reduced by 18%, 22% and 23% for DDQ, BH340 and DP490, respectively, in the RD. The tendencies in the RD, DD and TD are similar for all of the tested materials.

3.3. In-plane biaxial tension and unloading tests

In-plane biaxial tests were conducted using cruciform specimens with the machine designed by Kuwabara et al., 1998, as shown in Fig. 7. These test results were particularly useful to this study because the biaxial stress–strain data were accurately measured at small strains and an arbitrary load history such as unloading-reloading could be imposed. Arbitrary load ratios could be applied between the RD and TD of the sheet, but only the balanced biaxial loading condition was used in this study. Two pairs of strain gauges were attached to measure the strain along the RD and TD on both surfaces of the sheet, as shown in Fig. 7(b). The influence of bending strain, which originates from the initial curvature of the sheet, was eliminated by averaging the strains measured on the top and bottom surfaces of the sheet. The biaxial stress and thickness strain, corresponding to the effective stress and strain, respectively, are compared with the uniaxial tension data in Fig. 4. The hardening curves obtained from the two tests have similar shapes, but the stress is slightly higher in the biaxial tension curve for all of the tested materials.

The biaxial yield stress, σ_b, was determined such that it results in the same amount of plastic work as σ_0 in uniaxial tension. The plastic strain ratio, $r_b = \varepsilon^p_{yy}/\varepsilon^p_{xx}$, was determined by the linear regression of the measured plastic strain ratio between the RD and TD. These two properties are listed in Table 2. Note that the plastic strain ratio, r_b, was nearly constant throughout the test for all of the materials.

In addition to the monotonic tests, the loading–unloading–reloading tests were conducted at different amounts of applied biaxial stress. A pair of true stress–strain curves, $\sigma_{xx} - \varepsilon_{xx}$ and $\sigma_{yy} - \varepsilon_{yy}$, measured along the RD and TD, respectively, were obtained and are shown in Fig. 8. The initial and chord slopes were

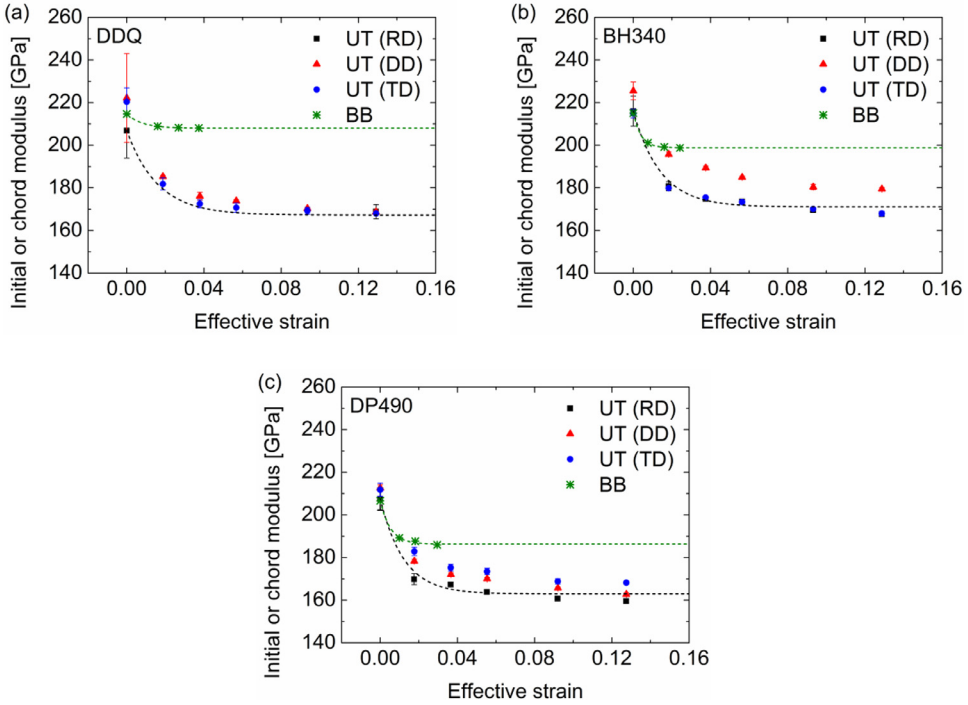

Fig. 6. Reduction of chord modulus as a function of effective strain measured in uniaxial tension (UT) and balanced biaxial tension (BB) for (a) DDQ, (b) BH340 and (c) DP490.

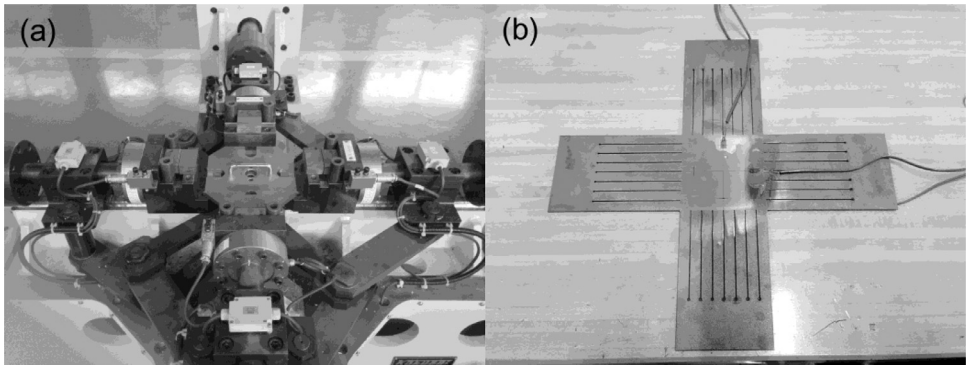

Fig. 7. (a) In-plane biaxial tester and (b) cruciform specimen.

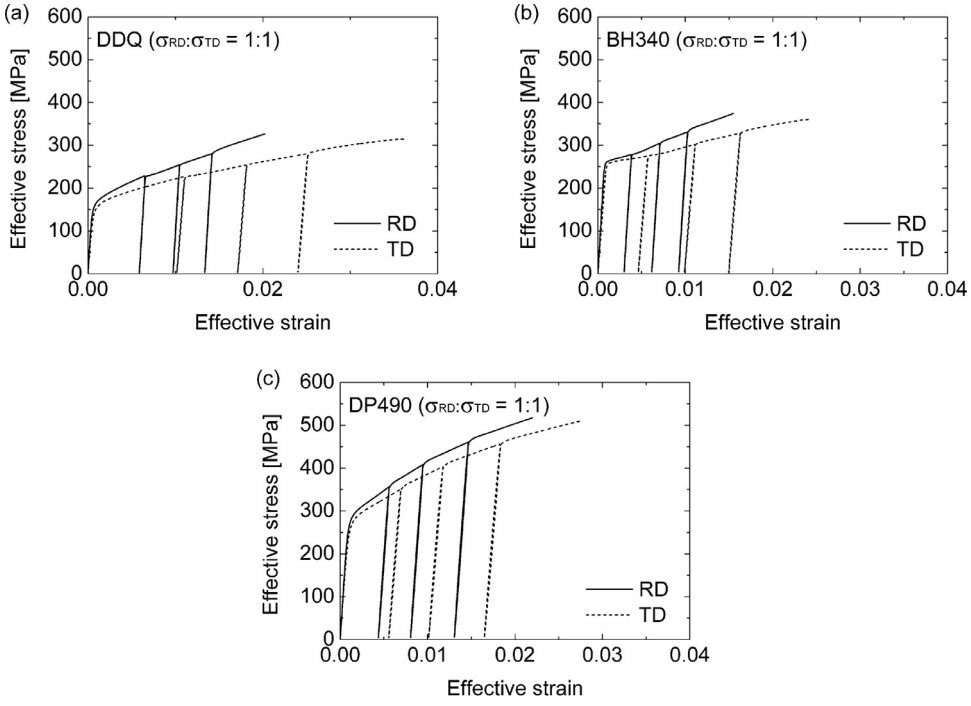

Fig. 8. True stress–strain components along the RD and TD in balanced biaxial loading–unloading–reloading tests for (a) DDQ, (b) BH340 and (c) DP490.

obtained from each curve, similar to the uniaxial case. It should be noted that these slopes do not correspond to the biaxial chord modulus. Assuming Hooke's law for isotropic elasticity in the plane stress condition ($\sigma_{zz} = 0$)

$$d\varepsilon^e_{xx} = (d\sigma_{xx} - \nu d\sigma_{yy})/E \tag{1a}$$

$$d\varepsilon^e_{yy} = (d\sigma_{yy} - \nu d\sigma_{xx})/E \tag{1b}$$

where the superscript e indicates the elastic component of the strain. When the balanced biaxial condition is imposed such that $\sigma_{xx} = \sigma_{yy}$, the above equations yield $d\sigma_{xx}/d\varepsilon^e_{xx} = d\sigma_{yy}/d\varepsilon^e_{yy} = E/(1-\nu)$. Although the measured slopes, $d\sigma_{xx}/d\varepsilon^e_{xx}$ and $d\sigma_{yy}/d\varepsilon^e_{yy}$, were different (24% for DDQ and 11% for DP490), their average was used as an approximation

$$(d\sigma/d\varepsilon^e)_{BB} = \left(d\sigma_{xx}/d\varepsilon^e_{xx} + d\sigma_{yy}/d\varepsilon^e_{yy}\right)/2 \tag{2}$$

and the corresponding chord modulus was obtained, assuming the above Hooke's laws and the Poisson ratio of 0.3

$$E_{BB} = (1-\nu)(d\sigma/d\varepsilon^e)_{BB} \tag{3}$$

The biaxial chord modulus, E_{BB}, is plotted as a function of the effective strain in Fig. 6. Its initial value is similar to that of uniaxial tension but its decrease as a function of strain is much lower for all of the tested materials.

3.4. Forward–reverse simple shear tests

Forward–reverse simple shear tests were performed using a simple shear device described by Choi (Choi, 2013). A 50 mm (RD) × 16 mm (TD) rectangular specimen was sheared along the RD, as described in the cited paper. The reverse shear stress–strain curves were obtained at pre-strains of approximately 2% and 5% in logarithmic (Hencky) shear strain, except for DDQ, for which only the 2% pre-strain data were available. The measured shear stress–strain data are shown in Fig. 9, which reveals typical reverse loading characteristics, such as the Bauschinger effect, transient hardening and permanent softening. Similar reverse loading behaviors are observed for the other two materials, except that permanent softening is not observed for DDQ.

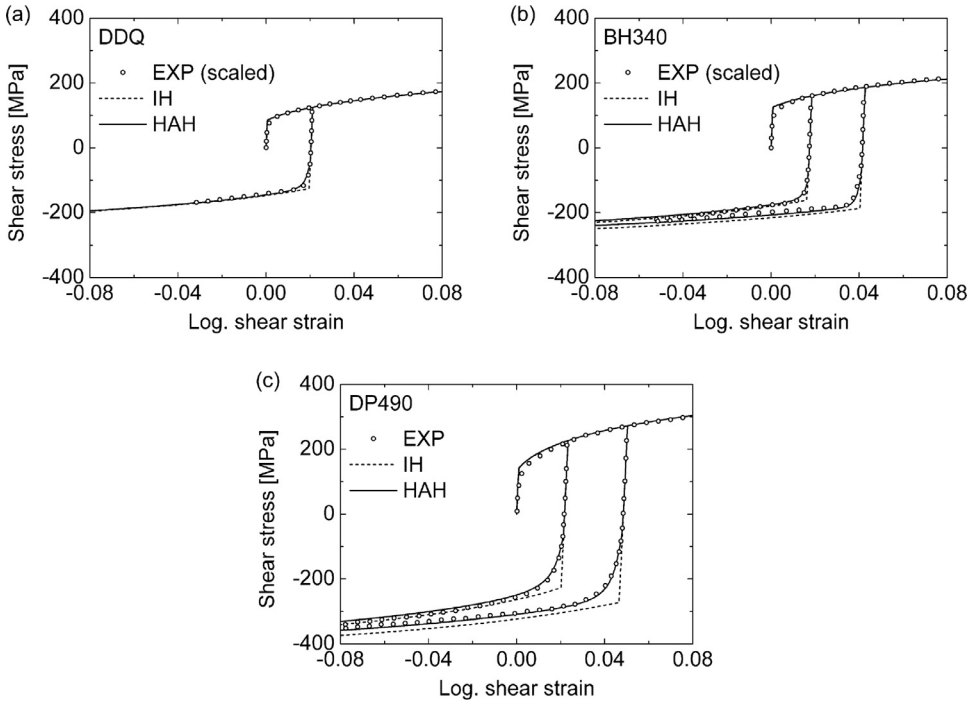

Fig. 9. Monotonic and reverse shear stress–strain curves for (a) DDQ, (b) BH340 and (c) DP490. Note that the measured stress–strain data for DDQ and BH340 were scaled to match with the Yld2000-2d prediction for parameter identification.

4. Constitutive modeling

4.1. Plastic anisotropy

The Yld2000-2d yield function involves eight parameters available using two linear transformations of the stress tensor in the plane stress condition (Barlat et al., 2003). A brief review of the theory and formulation is provided in Appendix B. The anisotropy parameters were determined using the uniaxial tension yield stresses and *r*-values along the three different loading directions, i.e., RD, DD and TD, as well as the biaxial yield stress and plastic strain ratio, which are given in Table 2. The anisotropy in both the yield stress and *r*-value are simultaneously captured using this model under the associated flow rule. The Newton–Raphson method was used to solve the eight nonlinear equations for parameter identification. The resulting parameters are listed in Table B1 (see Appendix B) for all of the materials and the predicted yield surface, for DP490 only, is shown in Fig. 10.

4.2. Hardening behavior

The monotonic hardening behavior of the materials was described using the Swift hardening law with the parameters approximated using the uniaxial tension curves, as shown in Fig. 4. The stress–strain data up to 10% effective strain were used for fitting to precisely capture the hardening behavior at small strains. As discussed in Section 2, the plastic deformation involved in denting rarely exceeds 10%.

The reverse hardening behavior was described using the homogeneous yield function-based anisotropic hardening (HAH) model (Barlat et al., 2011). This model describes hardening by the expansion and distortion of the yield surface to capture the complex anisotropic hardening response of metals under non-proportional loading, as explained in detail in Appendix C. For DDQ and BH340, because the monotonic shear stress–strain curve predictions did not match the experimental data, all the shear stress–strain data were calibrated by the same factor to fit the monotonic curve. The

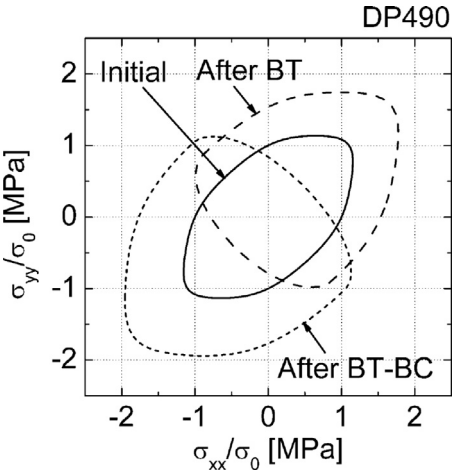

Fig. 10. Evolution of yield surface for DP490 under biaxial tension (BT) – biaxial compression (BC), predicted using the Yld2000-2d and HAH models. Yield surfaces are normalized by the initial yield stress in the RD.

HAH parameters, determined using these calibrated experimental data, are given in Table C1 (see Appendix C). As shown in Fig. 9, the Bauschinger effect, transient hardening and permanent softening are all captured using the HAH model. The expansion and distortion of the yield surface are illustrated in Fig. 10, where the evolution of the yield surface is predicted for DP490 for a loading sequence of 2% biaxial tension – 2% biaxial compression. As shown in the figure, the yield surface uniformly expands near the loading direction but flattens on the opposite side.

4.3. Elastic behavior

The strain-dependent elasticity model is adopted to describe the degradation of the chord modulus observed in Fig. 6. The uniaxial or biaxial moduli could be well fitted by the exponential

Fig. 11. Dent specimen with a dome height of 12 mm. The dent depth is less than 1 mm and hardly visible in the figure.

function (Yoshida et al., 2002)

$$E = E_0 - (E_0 - E_S)[1 - \exp(-\xi\bar{\varepsilon})] \quad (4)$$

where $\bar{\varepsilon}$ is the effective strain. E_0 denotes the initial modulus, E_S the saturated modulus and ξ the rate of reduction. These parameters were determined using either the uniaxial or biaxial moduli and are given in Table 3.

5. Prediction of load-displacement in the standard dent test

5.1. Standard dent tests

The standard dent tests, discussed in Section 2 and illustrated in Fig. 1, were conducted at POSCO (see Appendix A). First, dome-stretched panels were formed with two different punch strokes of 12 and 18 mm, resulting in approximately 2 and 5% of biaxial strain, respectively. Then, a dent load of 200 N was applied at the center of the formed panel at an indenter velocity of 2 mm/min. A tested sample is shown in Fig. 11. The load and displacement of the indenter were measured during the test, as shown in Fig. 12. The dent depth was calculated from the load-displacement curve as the difference between the indenter displacement at the reference load (2 N) during loading and unloading, as illustrated in Fig. 12(a). The calculated dent depths are given in Table 4.

5.2. Verification of the suggested model

The FE model described in Section 2 was used for the simulations. For verification purpose, the simulations were performed using two sets of constitutive models:

- Conventional model, assuming the isotropic von Mises yield criterion, isotropic hardening and a constant elastic modulus as measured during the initial loading in uniaxial tension along the RD.
- Advanced model, assuming the Yld2000-2d yield function, HAH hardening and chord models based on the biaxial elastic modulus.

It is common practice to use the uniaxial modulus to characterize the chord model. However, it seems more desirable to use the biaxial modulus in this example because the elastic responses in the dent region are in the biaxial stress state, as described in Section 2.

The predicted load-displacement responses are compared with the experimental data in Fig. 12. The simulations results show that the conventional model significantly overestimates the panel stiffness and underestimates the dent depth, especially for DDQ and DP490. The advanced model provides much improved predictions compared to the conventional model. This is also clear from Table 5, which compares the measured and predicted displacements at maximum (200 N) and intermediate (100 N) loads. Both the load-displacement history and the dent depth are predicted with greater accuracy for most cases, as shown in Table 4. These results clearly demonstrate the importance of comprehensive constitutive modeling in dent analysis.

The influences of plastic anisotropy, reverse hardening and elastic behaviors were separately investigated through additional simulations. Only the results for DP490 with a sample height of 12 mm are presented here, but similar trends were obtained for the other materials.

Influence of plastic anisotropy: FE simulations were performed using the HAH and chord model, based on the biaxial modulus, but the yield function was either the isotropic von Mises or the anisotropic Yld2000-2d. The simulation results are compared in Fig. 13(a), which shows that the Yld2000-2d model predicts higher stiffness than the von Mises. This is attributed to the higher yield stress predicted by Yld2000-2d in the balanced biaxial state, as shown in Fig. 10. This indicates that the description of biaxial yield stress directly influences the prediction of panel stiffness. It is interesting that for DP490 the biaxial yield stress is only 5% higher than the uniaxial stress, but this causes a noticeable difference in the load-displacement predictions. However, this amount of plastic anisotropy does not affect the dent depth.

Influence of reverse loading behavior: Simulations were performed using either isotropic hardening or the HAH model. The Yld2000-2d and chord models completed the constitutive description. The choice of the hardening model drastically changes the dent prediction, as shown in Fig. 13(b), especially regarding dent depth. In this figure, the isotropic hardening prediction (dashed curve) can be seen more clearly in the inset. The plastic deformation caused only by denting is 1%, implying that the accurate description of stress–strain behavior early in the reverse loading stage is highly important. It should be mentioned that the reverse shear stress–strain curves measured in this work may not accurately represent the actual biaxial tension-compression behavior involved in the dent test. For instance, it has been reported that the uniaxial tension-compression and forward-reverse simple shear stress–strain curves are different at the beginning of reverse loading (Choi, 2013).

Influence of elastic behavior: Simulations were performed using either the chord model based on the uniaxial modulus or the constant initial modulus, E_0, while keeping the chord model based on the biaxial modulus as a basis for comparisons. As expected, the elasticity model directly influences the panel stiffness, as shown in Fig. 13(c) and (d). If the chord model is characterized using the uniaxial modulus, which shows much more severe modulus reduction than the biaxial modulus (see Fig. 6), the predicted panel stiffness decreases, as shown in Fig. 13(c). If the initial modulus is used and the modulus reduction is ignored, the predicted panel stiffness increases, as shown in Fig. 13(d). These results indicate that the elastic properties should be described using a more comprehensive model than the conventional Hooke's law and the elastic degradation models based simply on the uniaxial modulus. Note also that the dent depth is hardly affected by the choice of elasticity model.

6. Discussions

The anisotropic (or kinematic) hardening and chord models have been widely used for springback analysis of sheet metals. In fact, springback examples have been used frequently to verify the validity of these models (Yoshida et al., 2002, Lee et al., 2012). However, model verification by springback analysis is not

Table 3
Parameters for the strain-dependent elasticity (chord) model.

	Based on uniaxial modulus (RD)			Based on biaxial modulus, E_{BB} in Eq. (3)		
	E_0 (GPa)	E_S (GPa)	ξ	E_0 (GPa)	E_S (GPa)	ξ
DDQ	207	167	63	215	208	125
BH340	216	171	71	215	199	258
DP490	207	163	82	207	185	191

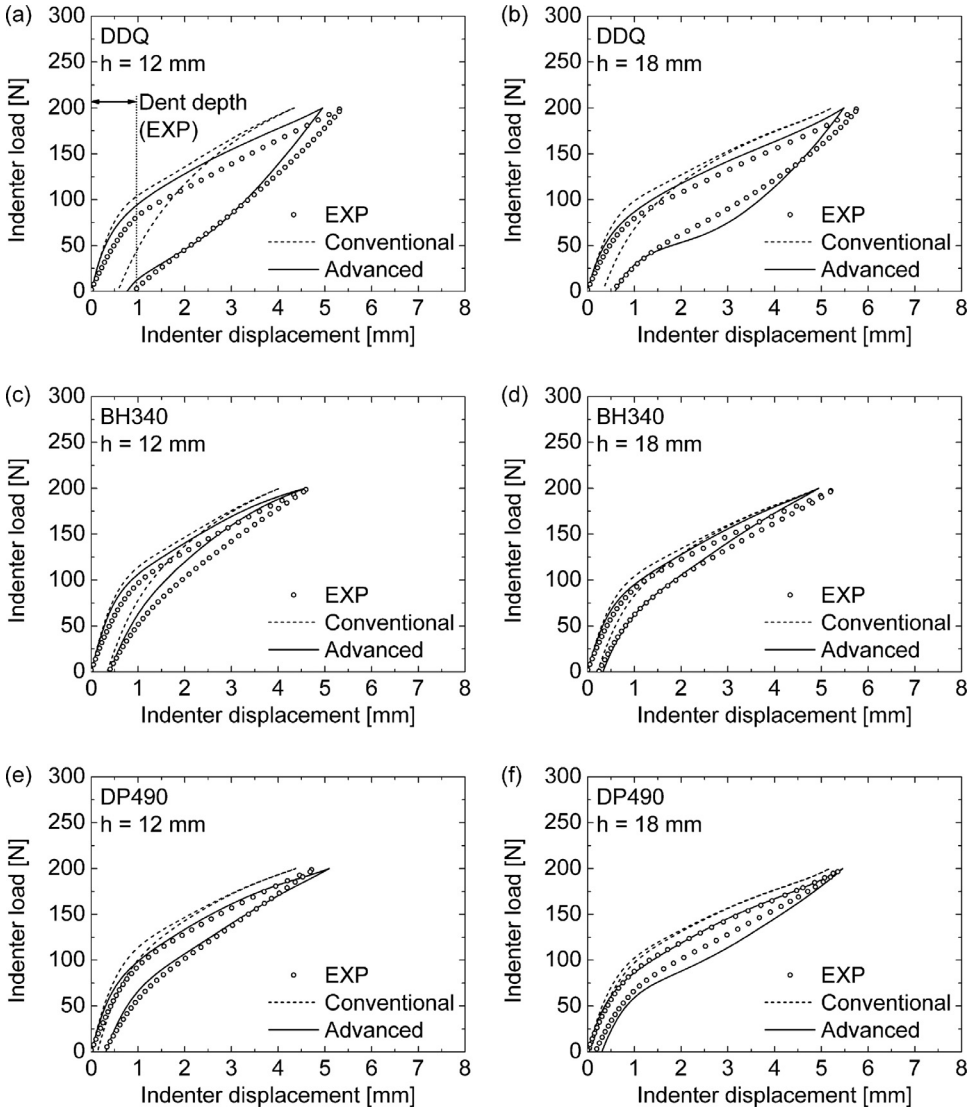

Fig. 12. Measured and predicted load-displacement responses in the standard dent tests for DDQ with sample heights (a) 12 mm and (b) 18 mm, for BH340 with (c) 12 mm and (d) 18 mm, and for DP490 with (c) 12 mm and (d) 18 mm.

Table 4
Measured and predicted dent depths, calculated using the reference load of 2 N. The numbers in parentheses indicate the prediction error: (prediction − experiment)/(experiment) × 100%.

	h = 12 mm			H = 18 mm		
	Experiment (mm)	Conventional (mm)	Advanced (mm)	Experiment (mm)	Conventional (mm)	Advanced (mm)
DDQ	0.98	0.57 (−42%)	0.78 (−20%)	0.59	0.33 (−44%)	0.60 (+2%)
BH340	0.40	0.34 (−15%)	0.40 (+0%)	0.26	0.22 (−15%)	0.33 (+27%)
DP490	0.30	0.13 (−57%)	0.31 (+3%)	0.19	0.06 (−68%)	0.31 (+63%)

Table 5
Measured and predicted indenter displacements at (a) the maximum load of 200 N, (b) 100 N during loading and (c) 100 N during unloading. The numbers in parentheses indicate the prediction error: (prediction– experiment)/(experiment) × 100%.

(a)	h = 12 mm			h = 18 mm		
	Experiment (mm)	Conventional (mm)	Advanced (mm)	Experiment (mm)	Conventional (mm)	Advanced (mm)
DDQ	5.36	4.34 (−19%)	4.95 (−8%)	5.80	5.23 (−10%)	5.48 (−5%)
BH340	4.66	4.03 (−13%)	4.58 (−2%)	5.31	4.94 (−7%)	4.94 (−7%)
DP490	4.77	4.38 (−8%)	5.09 (+7%)	5.43	5.18 (−5%)	5.46 (+0%)
(b)	h = 12 mm			h = 18 mm		
	Experiment (mm)	Conventional (mm)	Advanced (mm)	Experiment (mm)	Conventional (mm)	Advanced (mm)
DDQ	1.56	0.88 (−44%)	1.12 (−28%)	1.69	1.04 (−39%)	1.38 (−18%)
BH340	1.08	0.73 (−32%)	0.86 (−20%)	1.24	0.91 (−27%)	1.13 (−9%)
DP490	1.15	0.75 (−34%)	1.03 (−10%)	1.32	0.95 (−28%)	1.39 (+5%)
(c)	h = 12 mm			h = 18 mm		
	Experiment (mm)	Conventional (mm)	Advanced (mm)	Experiment (mm)	Conventional (mm)	Advanced (mm)
DDQ	3.36	1.70 (−49%)	3.31 (−1%)	3.33	1.56 (−53%)	3.69 (+11%)
BH340	1.94	1.30 (−33%)	1.59 (−18%)	1.89	1.30 (−31%)	1.86 (−2%)
DP490	1.96	1.00 (−49%)	1.80 (−8%)	1.96	1.06 (−46%)	2.50 (+28%)

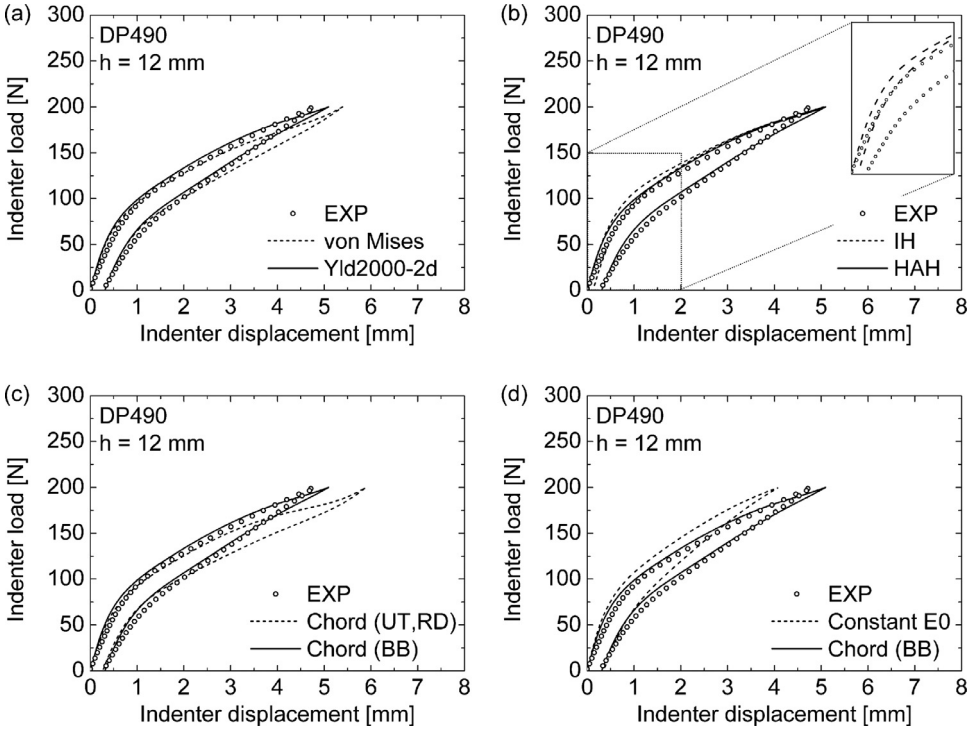

Fig. 13. Changes in dent prediction using different choices of (a) yield function, (b) hardening law, (c) and (d) elasticity model. The isotropic hardening (IH) prediction in (b) can be seen more clearly in the inset.

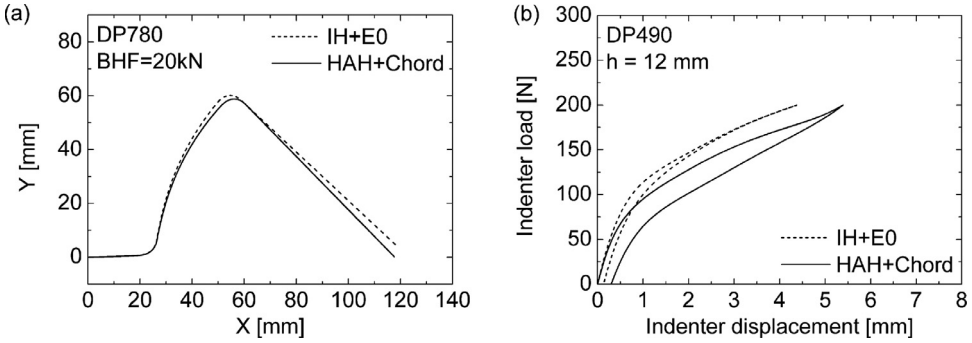

Fig. 14. (a) Predicted springback profiles for DP780 in U-draw/bending with a blank holding force of 20 kN and (b) predicted load-displacement in the standard dent test for DP490 (IH: isotropic hardening and E_0: initial elastic modulus). The von Mises yield criterion was used in both examples.

straightforward and might lead to erroneous conclusions. An example is shown in Fig. 14(a), which compares the springback profiles after U-draw/bending (Numiform'93 benchmark (Taylor et al., 1995)) predicted using two sets of models: (1) isotropic hardening and initial elastic modulus and (2) the HAH and chord models. Although the former cannot capture the reverse loading and elastic degradation behaviors as the latter does, both generate similar springback predictions. This can be understood simply, knowing that a material with higher strength and lower elastic modulus generally experiences larger springback. Isotropic hardening, which overestimates the reverse yield stress, predicts larger springback than the HAH (or kinematic hardening) model. On the contrary, the use of the initial elastic modulus predicts smaller springback than the chord model. Therefore, when isotropic hardening and initial modulus are used together, the errors induced by these models compensate for each other, thus providing results similar to those with the combination of the HAH and chord models. This is why the conventional model, which captures neither the Bauschinger effect nor the change of elastic modulus, sometimes provides a surprisingly accurate, but coincidental, springback prediction.

Dent predictions also depend strongly on the choice of the hardening and elasticity models. However, unlike springback predictions, the effects of these two models do not compensate for each other. As demonstrated in Fig. 13, the hardening model mainly influences the predicted dent depth, while the elasticity model does the overall stiffness. Therefore, combining isotropic hardening and initial modulus leads to results entirely different from those predicted by the HAH and chord models, as shown in Fig. 14(b). An accurate prediction is possible only when comprehensive constitutive models are used, and this makes the dent analysis a good example for model verification. It is also worth mentioning that the dent analysis is not as sensitive to friction as the springback analysis, which is strongly affected by the friction model (Lee et al., 2015).

7. Conclusions

In this study, the quasi-static dent behaviors of DDQ, BH340 and DP490 steel sheets were predicted using the conventional and advanced constitutive models. The latter provided more accurate predictions than the former. The sensitivity study provided the following conclusions:

- Accurate descriptions of plastic anisotropy, reverse loading and elastic behaviors of the material are essential for accurate dent predictions.
- The plastic anisotropy and elastic behavior strongly influence the panel stiffness and the reverse loading behavior affects the dent depth.
- It is particularly important to consider the biaxial elastic modulus of the material, which is often simplified to the uniaxial modulus.

Further improvement to the constitutive model is expected by investigating the reverse hardening behavior in different stress states, such as biaxial tension–compression. In addition, the extension of the elastic degradation model to incorporate elastic anisotropy, capturing both uniaxial and biaxial moduli, may contribute to better predictions.

Acknowledgments

This research was supported by POSCO. This work was partially supported by the National Research Foundation of Korea (NRF) grant funded by the Korea government (MSIP) (no.2012R1A5A1048294) and (NRF-2014R1A2A1A11052889). FB appreciates the support of FEDER funds through the Operational Program for Competitiveness Factors – COMPETE and National Funds through the Portuguese FCT – Foundation for Science and Technology under the projects PTDC/EMS-TEC/2404/2012. Jisik Choi and Ahmad Zadi Maad from GIFT-POSTECH are appreciated for their supports for the shear and in-plane biaxial tests. Jeong-Yeon Lee appreciates the support from Korea University Grant.

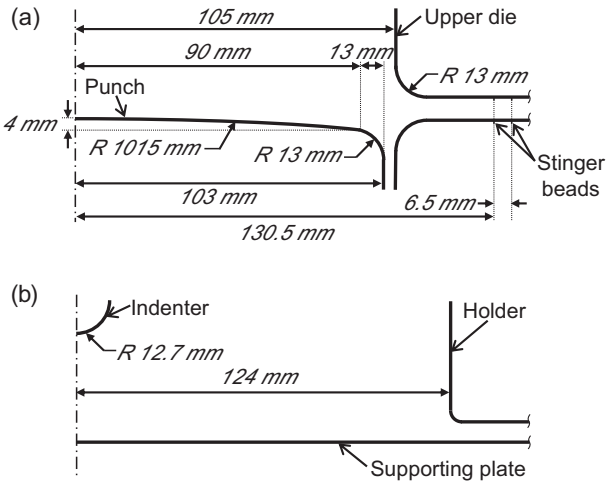

Fig. A1. Tool geometry for the standard dent test for (a) pre-stretching and (b) denting. The dash-dotted line denotes the axis of axisymmetry.

Appendix A. Tool geometry for the standard dent test

The tool geometry for the standard dent test used in this work generally follows the descriptions given in the SAE J2575 standard (SAE, 2004). However, the geometry of the punch used in the pre-stretching process is ambiguously defined in the cited document. The text defines the punch radius on the plateau as 940 mm, whereas the supplementary drawing defines it as 1015 mm. The equipment used in this study was built according to the drawing, thus the FE model uses a punch radius of 1015 mm. This is illustrated in Fig. A1. Note that the corner radii of the lower die (for pre-stretching, see Fig. A1(a)) and that of the holder (for denting, see Fig. A1(b)) do not require specifications, because the panel does not touch these corners.

Appendix B. Non-quadratic anisotropic yield function for plane stress (Yld2000-2d)

The Yld2000-2d yield function is expressed as follows (Barlat et al., 2003):

$$\phi = \left(\frac{\phi' + \phi''}{2}\right)^{1/m} = \bar{\sigma} \tag{B1}$$

where

$$\phi' = \left|X_1' - X_2'\right|^m \text{ and } \phi'' = \left|2X_2'' + X_1''\right|^m + \left|2X_1'' + X_2''\right|^m \tag{B2}$$

Here, X_1' and X_2' are the two principal values of a linearly transformed tensor $\boldsymbol{X'} = \boldsymbol{L'\sigma}$ ($\boldsymbol{\sigma}$ is the Cauchy stress tensor). Similarly, X_1'' and X_2'' are defined using $\boldsymbol{X''} = \boldsymbol{L''\sigma}$,

$$\begin{bmatrix} X_{xx}' \\ X_{yy}' \\ X_{xy}' \end{bmatrix} = \begin{bmatrix} L_{11}' & L_{12}' & 0 \\ L_{21}' & L_{22}' & 0 \\ 0 & 0 & L_{66}' \end{bmatrix} \begin{bmatrix} \sigma_{xx} \\ \sigma_{yy} \\ \sigma_{xy} \end{bmatrix} \tag{B3a}$$

$$\begin{bmatrix} X_{xx}'' \\ X_{yy}'' \\ X_{xy}'' \end{bmatrix} = \begin{bmatrix} L_{11}'' & L_{12}'' & 0 \\ L_{21}'' & L_{22}'' & 0 \\ 0 & 0 & L_{66}'' \end{bmatrix} \begin{bmatrix} \sigma_{xx} \\ \sigma_{yy} \\ \sigma_{xy} \end{bmatrix} \tag{B3b}$$

Table B1
Yld2000-2d yield function parameters. The exponent m was assumed to be 6.

	α_1	α_2	α_3	α_4	α_5	α_6	α_7	α_8
DDQ	0.9331	1.1038	1.1520	0.9571	0.9115	0.6178	0.9936	0.9308
BH340	0.8406	1.2766	0.8992	0.9654	0.9301	0.6814	0.9594	1.1136
DP490	0.8193	1.1147	0.9958	0.9841	0.9804	0.7479	0.9834	1.1096

Table C1
Swift and HAH model parameters.

	Swift			HAH				
	K(MPa)	ε_0	n	k_1	k_2	k_3	k_4	k_5
DDQ	626.12	0.009	0.3	220	150	0.3	1.0	0
BH340	645.18	0.012	0.245	250	80	0.5	0.9	20
DP490	1026.82	0.005	0.267	110	150	0.3	0.9	17

The transformation operators $\boldsymbol{L}'$ and $\boldsymbol{L}''$ contain three and five independent anisotropy parameters, respectively, which are denoted as $\alpha_1 - \alpha_8$

$$\begin{bmatrix} L'_{11} \\ L'_{12} \\ L'_{21} \\ L'_{22} \\ L'_{66} \end{bmatrix} = \begin{bmatrix} 2/3 & 0 & 0 \\ -1/3 & 0 & 0 \\ 0 & -1/3 & 0 \\ 0 & 2/3 & 0 \\ 0 & 0 & 1 \end{bmatrix} \begin{bmatrix} \alpha_1 \\ \alpha_2 \\ \alpha_7 \end{bmatrix} \tag{B4a}$$

$$\begin{bmatrix} L''_{11} \\ L''_{12} \\ L''_{21} \\ L''_{22} \\ L''_{66} \end{bmatrix} = \frac{1}{9} \begin{bmatrix} -2 & 2 & 8 & -2 & 0 \\ 1 & -4 & -4 & 4 & 0 \\ 4 & -4 & -4 & 1 & 0 \\ -2 & 8 & 2 & -2 & 0 \\ 0 & 0 & 0 & 0 & 0 \end{bmatrix} \begin{bmatrix} \alpha_3 \\ \alpha_4 \\ \alpha_5 \\ \alpha_6 \\ \alpha_8 \end{bmatrix} \tag{B4b}$$

The eight parameters can be determined using the uniaxial tension yield stresses and r-values along the RD, DD and TD, as well as the biaxial tension yield stress and plastic strain ratio ($r_b = \varepsilon^p_{yy}/\varepsilon^p_{xx}$). The parameters determined for DDQ, BH340 and DP490 are given in Table B1. Note that, when m equals 2 and α_1 through α_8 equal 1, the yield function reduces to the von Mises.

Appendix C. Homogeneous yield function-based anisotropic hardening (HAH) model

The original HAH model expresses the yield function as a combination of stable ϕ and fluctuating ϕ_h parts (Barlat et al., 2011)

$$\begin{aligned} \Phi(\boldsymbol{s}) &= \left[\phi^q + \phi_h^q\right]^{\frac{1}{q}} \\ &= \left[\phi^q + f_1^q \left|\hat{\boldsymbol{h}}^{\boldsymbol{s}} : \boldsymbol{s} - \left|\hat{\boldsymbol{h}}^{\boldsymbol{s}} : \boldsymbol{s}\right|\right|^q + f_2^q \left|\hat{\boldsymbol{h}}^{\boldsymbol{s}} : \boldsymbol{s} + \left|\hat{\boldsymbol{h}}^{\boldsymbol{s}} : \boldsymbol{s}\right|\right|^q\right]^{\frac{1}{q}} = \bar{\sigma} \end{aligned} \tag{C1}$$

Any homogeneous yield function of degree one, in the form of $\phi(\boldsymbol{s}) = \bar{\sigma}$, can be used for the stable component. The fluctuating component is introduced to induce a yield surface distortion and is a function of the stress deviator $\boldsymbol{s}$, microstructure deviator $\hat{\boldsymbol{h}}^{\boldsymbol{s}}$, and state variables f_1 and f_2. The microstructure deviator memorizes the previous loading history and is defined as a normalized traceless tensor as

$$\hat{\boldsymbol{h}}^{\boldsymbol{s}} = \frac{\boldsymbol{h}^{\boldsymbol{s}}}{\sqrt{(8/3)\boldsymbol{h}^{\boldsymbol{s}} : \boldsymbol{h}^{\boldsymbol{s}}}} \tag{C2}$$

When the plastic deformation initiates, $\boldsymbol{h}^{\boldsymbol{s}}$ is set equal to $\boldsymbol{s}$. As the deformation path changes, $\boldsymbol{h}^{\boldsymbol{s}}$ also changes gradually toward the stress deviator corresponding to the new loading direction at a rate controlled by a parameter k

If $\boldsymbol{s} : \hat{\boldsymbol{h}}^{\boldsymbol{s}} \geq 0$,

$$\frac{d\hat{\boldsymbol{h}}^{\boldsymbol{s}}}{d\bar{\varepsilon}} = k\left[\hat{\boldsymbol{s}} - \frac{8}{3}\hat{\boldsymbol{h}}^{\boldsymbol{s}}(\hat{\boldsymbol{s}} : \hat{\boldsymbol{h}}^{\boldsymbol{s}})\right] \tag{C3a}$$

If $\boldsymbol{s} : \hat{\boldsymbol{h}}^{\boldsymbol{s}} < 0$,

$$\frac{d\hat{\boldsymbol{h}}^{\boldsymbol{s}}}{d\bar{\varepsilon}} = k\left[-\hat{\boldsymbol{s}} + \frac{8}{3}\hat{\boldsymbol{h}}^{\boldsymbol{s}}(\hat{\boldsymbol{s}} : \hat{\boldsymbol{h}}^{\boldsymbol{s}})\right] \tag{C3b}$$

where $\hat{\boldsymbol{s}}$ is equivalent to $\boldsymbol{s}$ but normalized in the manner of Eq. (C2).

The microstructure deviator controls the direction of yield surface distortion, and the state variables f_1 and f_2 control the amount and rate of distortion. These are functions of g_1 and g_2, which represent the ratio of the current flow stress to that of the hypothetical associated isotropic hardening material

$$f_1 = \left[g_1^{-q} - 1\right]^{1/q} \text{ and } f_2 = \left[g_2^{-q} - 1\right]^{1/q} \tag{C4}$$

In the initial state, the fluctuating component do not contribute to the yield function, and the yield function Φ is the same as the stable component ϕ. Therefore, $f_1 = f_2 = 0$, or equivalently, $g_1 = g_2 = 1$. If the material plastically deforms, the state variables evolve according to the following relationships:

If $\boldsymbol{s} : \hat{\boldsymbol{h}}^{\boldsymbol{s}} \geq 0$,

$$\frac{dg_1}{d\bar{\varepsilon}} = k_2\left[k_3\frac{\bar{\sigma}(0)}{\bar{\sigma}(\bar{\varepsilon})} - g_1\right] \tag{C5}$$

$$\frac{dg_2}{d\bar{\varepsilon}} = k_1\frac{g_3 - g_2}{g_2} \tag{C6}$$

$$\frac{dg_4}{d\bar{\varepsilon}} = k_5(k_4 - g_4) \tag{C7}$$

If $\boldsymbol{s} : \hat{\boldsymbol{h}}^{\boldsymbol{s}} < 0$,

$$\frac{dg_1}{d\bar{\varepsilon}} = k_1\frac{g_4 - g_1}{g_1} \tag{C8}$$

$$\frac{dg_2}{d\bar{\varepsilon}} = k_2\left[k_3\frac{\bar{\sigma}(0)}{\bar{\sigma}(\bar{\varepsilon})} - g_2\right] \tag{C9}$$

$$\frac{dg_3}{d\bar{\varepsilon}} = k_5(k_4 - g_3) \tag{C10}$$

Here, $\bar{\sigma}(\bar{\varepsilon})$ is the monotonic hardening curve and $k_1 - k_5$ are the material parameters. Two additional state variables, g_3 and g_4, are introduced to describe permanent softening. If $k_4 = 1$ (or $k_5 = 1$) and $g_3 = g_4 = 1$, the model predicts no permanent softening.

The monotonic hardening curve $\bar{\sigma} = \bar{\sigma}(\bar{\varepsilon})$ should be defined in the model. If the material is subjected only to monotonic loading, the stress–strain behavior described by the HAH model is identical to that by isotropic hardening. In this work, the Swift hardening law is employed for monotonic hardening

$$\bar{\sigma}(\bar{\varepsilon}) = K(\varepsilon_0 + \bar{\varepsilon})^n \tag{C11}$$

The parameters K, ε_0 and n were obtained by fitting the uniaxial tension data measured along the RD. Since the dent analysis does not involve large strains, the stress–strain data up to 10% strain were used for the fitting, as shown in Fig. 4. These parameters are given in Table C1.

For the HAH model, the recommended values were used for $q = 2$ and $k = 30$ (Barlat et al., 2011), and the other parameters k_1–k_5 were determined using the reverse shear stress–strain data, as shown in Fig. 9 for DP490. For DDQ and BH340 the monotonic shear stress–strain curve predictions did not match the experimental data, and all the shear stress–strain data were calibrated by the same factor to fit the monotonic stress–strain curve. The HAH parameters were then determined using these calibrated experimental data. The determined parameters are given in Table C1.

References

ASTM, 2010. ASTM E8/E8M: Standard test methods for tension testing of metallic materials.

Barlat, F., Brem, J.C., Yoon, J.W., Chung, K., Dick, R.E., Lege, D.J., Pourboghrat, F., Choi, S.H., Chu, E., 2003. Plane stress yield function for aluminum alloy sheets – Part 1: theory. Int. J. Plast. 19, 1297–1319.

Barlat, F., Gracio, J.J., Lee, M.G., Rauch, E.F., Vincze, G., 2011. An alternative to kinematic hardening in classical plasticity. Int. J. Plast. 27, 1309–1327.

Chaboche, J.L., 1986. Time-independent constitutive theories for cyclic plasticity. Int. J. Plast. 2, 149–188.

Choi, J., 2013. Simple Shear Flow Behavior For Advanced High Strength Steel (AHSS) Sheets Master Thesis. Pohang University of Science and Technology, Pohang, Republic of Korea.

Cleveland, R.M., Ghosh, A.K., 2002. Inelastic effects on springback in metals. Int. J. Plast. 18, 769–785.

Dicello, J.A., George, R.A., 1974. Design Criteria for the Dent Resistance of Auto Body Panels, 740081, Technical Papers, SAE.

Eggertsen, P.-A., Mattiasson, K., Hertzman, J., 2011. A phenomenological model for the hysteresis behavior of metal sheets subjected to unloading/reloading cycles. J. Manuf. Sci. Eng. 133, 061021.

Hill, R., 1948. A theory of the yielding and plastic flow of anisotropic metals. Proc. R. Soc. Lond. 193, 281–297.

Holmberg, S., Nejabat, B., 2004. Numerical assessment of stiffness and dent properties of automotive exterior panels. Mater. Des. 25, 361–368.

Kuwabara, T., Ikeda, S., Kuroda, K., 1998. Measurement and analysis of differential work hardening in cold-rolled steel sheet under biaxial tension. J. Mater. Process. Tech. 80–81, 517–523.

Lee, J.W., Lee, M.G., Barlat, F., 2012. Finite element modeling using homogeneous anisotropic hardening and application to spring-back prediction. Int. J. Plast. 29, 13–41.

Lee, J.Y., Barlat, F., Lee, M.G., 2015. Constitutive and friction modeling for accurate springback analysis of advanced high strength steel sheets. Int. J. Plast. 71, 113–135.

SAE, 2004. Surface Vehicle Standard J2575: Standardized Dent Resistance Test Procedure.

Shen, H., Li, S., Chen, G., 2010. Numerical analysis of panels' dent resistance considering the Bauschinger effect. Mater. Des. 31, 870–876.

Sun, L., Wagoner, R.H., 2011. Complex unloading behavior: nature of the deformation and its consistent constitutive representation. Int. J. Plast. 27, 1126–1144.

Taylor, L., Cao, J., Karafillis, A.P., Boyce, M.C., 1995. Numerical simulations of sheet-metal forming. J. Mater. Process. Tech. 50, 168–179.

van Veldhuizen, B., Kranendonk, W., Ruifrok, R., 1995. The relation between the curvature of horizontal automotive panels, the panel stiffness and the static dent resistance. In: Proceedings of the International Body Engineering Conference. Detroit, Michigan, USA, pp. 62–70.

Yoshida, F., Uemori, T., Fujiwara, K., 2002. Elastic-plastic behavior of steel sheets under in-plane cyclic tension-compression at large strain. Int. J. Plast. 18, 633–659.